ARTICLE

Structure of the toxic core of α–synuclein from invisible crystals

Jose A. Rodriguez[1]*, Magdalena I. Ivanova[1]*†, Michael R. Sawaya[1]*, Duilio Cascio[1]*, Francis E. Reyes[2]*, Dan Shi[2], Smriti Sangwan[1], Elizabeth L. Guenther[1], Lisa M. Johnson[1], Meng Zhang[1], Lin Jiang[1]†, Mark A. Arbing[1], Brent L. Nannenga[2], Johan Hattne[2], Julian Whitelegge[3], Aaron S. Brewster[4], Marc Messerschmidt[5]†, Sébastien Boutet[5], Nicholas K. Sauter[4], Tamir Gonen[2] & David S. Eisenberg[1]

The protein α–synuclein is the main component of Lewy bodies, the neuron-associated aggregates seen in Parkinson disease and other neurodegenerative pathologies. An 11-residue segment, which we term NACore, appears to be responsible for amyloid formation and cytotoxicity of human α–synuclein. Here we describe crystals of NACore that have dimensions smaller than the wavelength of visible light and thus are invisible by optical microscopy. As the crystals are thousands of times too small for structure determination by synchrotron X-ray diffraction, we use micro-electron diffraction to determine the structure at atomic resolution. The 1.4 Å resolution structure demonstrates that this method can determine previously unknown protein structures and here yields, to our knowledge, the highest resolution achieved by any cryo-electron microscopy method to date. The structure exhibits protofibrils built of pairs of face-to-face β-sheets. X-ray fibre diffraction patterns show the similarity of NACore to toxic fibrils of full-length α–synuclein. The NACore structure, together with that of a second segment, inspires a model for most of the ordered portion of the toxic, full-length α–synuclein fibril, presenting opportunities for the design of inhibitors of α–synuclein fibrils.

The presynaptic protein α-synuclein, found in both soluble and membrane-associated fractions of the brain, aggregates in Parkinson disease (PD). These aggregates are the main component of Lewy bodies, the defining histological feature of this neurodegenerative disease, and have been shown to accompany neuronal damage[1]. Two other observations point to aggregated α-synuclein as a molecular cause of PD[2]. The first is that families with inherited forms of PD carry mutations in α-synuclein, such as A53T, and abundant Lewy bodies[3–5]. The second is that families with duplicated or triplicated genes encoding α-synuclein develop early-onset PD, presumably because at high local concentrations α-synuclein is forced into amyloid[6,7].

Our focus is on a central segment of α-synuclein, residues 68–78, that we term NACore (Fig. 1), because of its critical role in both the aggregation and cytotoxicity of α-synuclein. NACore lies within a 35-residue domain of α-synuclein termed NAC (non-amyloid-β component, originally reported to be deposited with amyloid-β in the brains of Alzheimer's disease patients), which has been established as necessary and sufficient for the aggregation and toxicity of α-synuclein[8–12] (Extended Data Fig. 1). For example, deletion of residues 71–82 prevents aggregation of α-synuclein in vitro, and abolishes both its aggregation and neurotoxicity in a Drosophila model of PD[12]. Yet this segment in isolation from the rest of α-synuclein readily forms amyloid fibrils and is highly cytotoxic[13,14]. Also, β-synuclein, the close homologue of α-synuclein, which does not aggregate and is not found in Lewy bodies, differs in sequence from α-synuclein principally by the lack of residues 74–84 that are part of NACore[9].

Segments outside NAC also influence the aggregation of α-synuclein and have been associated with fibril structure[15–17]. In brain extracts from patients with multiple system atrophy, the core of α-synuclein fibrils extends approximately from residue 30 to 100[18]. Also the A53T mutation of α-synuclein can accelerate its transition into the amyloid state, and hence accelerate PD[19]. This mutation was found to induce the onset of PD at an early age[20], and consistent with this, α-synuclein containing this A53T mutation forms fibrils in vitro more rapidly than the wild type[3]. Thus we carried out screens for crystals of peptide segments within the NAC domain and adjacent regions, seeking structural information on the molecular basis of aggregation and toxicity of α-synuclein.

Structure determination by MicroED

Extensive crystal screens of two segments, NACore, residues 68GAVVTGVTAVA78, and PreNAC, 47GVVHGVTTVA56, seemingly produced non-crystalline, amorphous aggregates. But upon examination using electron microscopy, we found the aggregates to be clusters of elongated nanocrystals only 50–300 nm in cross section and thus invisible by conventional light microscopy (Fig. 1). We confirmed well-ordered crystallinity of NACore at both the SACLA and LCLS free electron lasers. We also found that a nine-residue fragment within the NACore, which we term SubNACore, 69AVVTGVTAV77, yielded crystals 1,000–10,000 times larger in volume than the NACore nanocrystals (Fig. 1). We were therefore able to apply synchrotron methods[21,22] to these larger crystals to determine the structure of their amyloid-like fibrils. Although this nine-residue fragment is missing only two residues compared with NACore, it is not as toxic[23], offering some insight into the toxicity of α-synuclein, as described below.

To determine the structure of the invisible crystals of NACore and PreNAC, we turned to micro-electron diffraction (MicroED)[24–26]. In
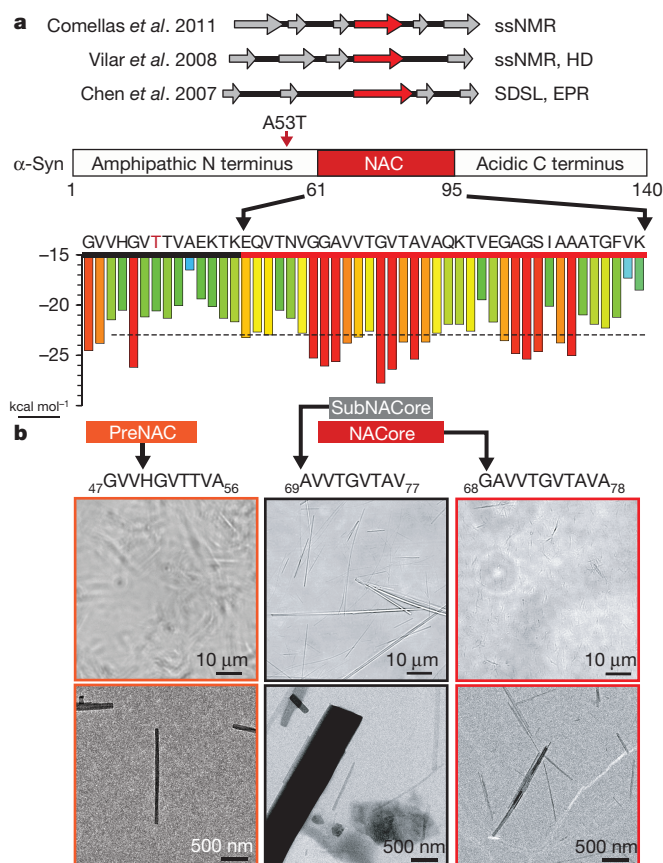
Figure 1 | NACore (residues 68–78) is the fibril-forming core of the NAC domain of full-length α-synuclein. a, Top, segments identified as β-strands by electron paramagnetic resonance (EPR), solid state nuclear magnetic resonance (ssNMR), hydrogen-deuterium exchange (HD), and site directed spin labelling (SDSL)[17,40,41]. Bottom, predictions of the propensity of six-residue segments to form amyloid fibrils. The vertical axis indicates the propensity of steric zipper formation in Rosetta energy units[42]. Zipper-forming segments are predicted where bars cross the -23 kcal mol^{-1} threshold marked by the dashed line. Blue-to-red color gradient indicates weak-to-strong propensity of steric zipper formation. The A53T early-onset Parkinson mutation is indicated by a red arrow and red letter T. **b**, The miniscule size of the preNAC and NACore crystals used for MicroED is illustrated by this comparison to SubNACore microcrystals. Scale comparisons are illustrated on two magnifications using phase contrast light microscope images and electron micrographs, in which individual NACore and PreNAC nanocrystals are indistinguishable by light microscopy.

MicroED, an extremely low-dose electron beam is directed onto a nanocrystal within a transmission electron microscope under cryogenic conditions, yielding diffraction patterns such as those in Fig. 2. As the wavelength used in our experiments at 200 keV is very small (0.025 Å), the Ewald sphere is essentially flat, resulting in diffraction patterns that closely resemble a 2D slice through 3D reciprocal space. As the crystal is continuously rotated in the beam, a series of such diffraction patterns is collected[25]. Scaling together diffraction data collected from multiple crystals produces a full 3D diffraction data set. MicroED has been successfully applied to the well-known structures of hen egg-white lysozyme[25,26], bovine liver catalase[27] and Ca^{2+}-ATPase[28]. But NACore and PreNAC are the first previously unknown structures determined by MicroED.

For NACore and PreNAC, we collected MicroED patterns from nano-crystals that lay preferentially oriented, flat on the surface of a holey carbon Quantifoil grid, in a frozen-hydrated state. Grids were first screened for appropriately sized crystals, and candidate crystals screened for diffraction. We used crystals showing strong diffraction for data collection by continuous unidirectional rotation about a fixed
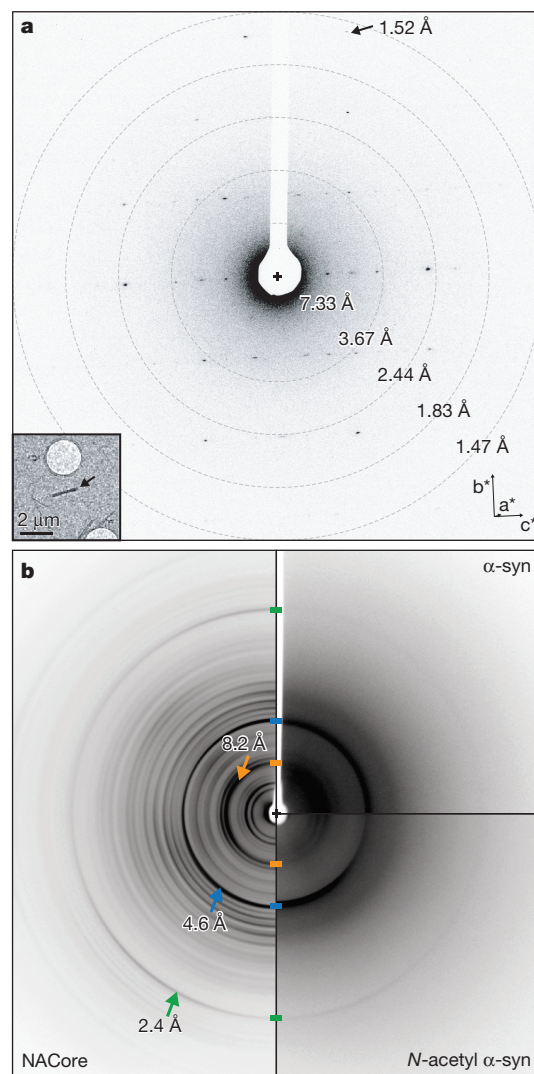

Figure 2 | Diffraction from NACore nanocrystals is similar to that from full length α-synuclein fibrils. a, Single-crystal electron diffraction pattern obtained during MicroED data collection (see text). Equally spaced concentric rings denote resolution shells. The highest resolution spot is at 1.52 Å (arrow). The inset shows the over-focused image of the diffracting crystal (arrow), which is ~1,480 × 200 × 200 nm. Orientation of the reciprocal cell axes are indicated by the arrows labelled a*, b*, c*. **b**, Composite of fibril diffraction patterns from α-synuclein (α-syn) preparations and NACore. Full-length α-synuclein reveals reflections that match those from NACore and N-terminally acetylated α-synuclein. The two patterns of full-length α-synuclein share with NACore three major peaks denoted by arrows: 8.2 Å (orange), 4.6 Å (blue), and 2.4 Å (green). The origin of these peaks can be traced to the (0,0,2), [(1,1,1),(−1,1,1)], and (0,2,0) planes in the NACore structure, respectively. We attribute the strong 8.2 Å reflection to the spacing between adjacent pairs of β-sheets.

axis, acquiring a series of diffraction frames at fixed time intervals[25]. The needle-shaped crystals typically exceeded the length needed for MicroED; those that were unbent and 100 to 300 nm wide produced the best diffraction patterns. Data from multiple crystals were integrated, scaled and merged together (Extended Data Table 1).

The multi-crystal NACore and PreNAC data sets were phased by molecular replacement, using the atomic model of SubNACore and an ideal β-strand model, respectively, as probes. Residues of NACore which were missing from the SubNACore probe were clearly revealed in a difference density map calculated from NACore observed structure factor amplitudes and phases from the SubNACore probe structure (Extended Data Fig. 2). After subsequent refinement, two water
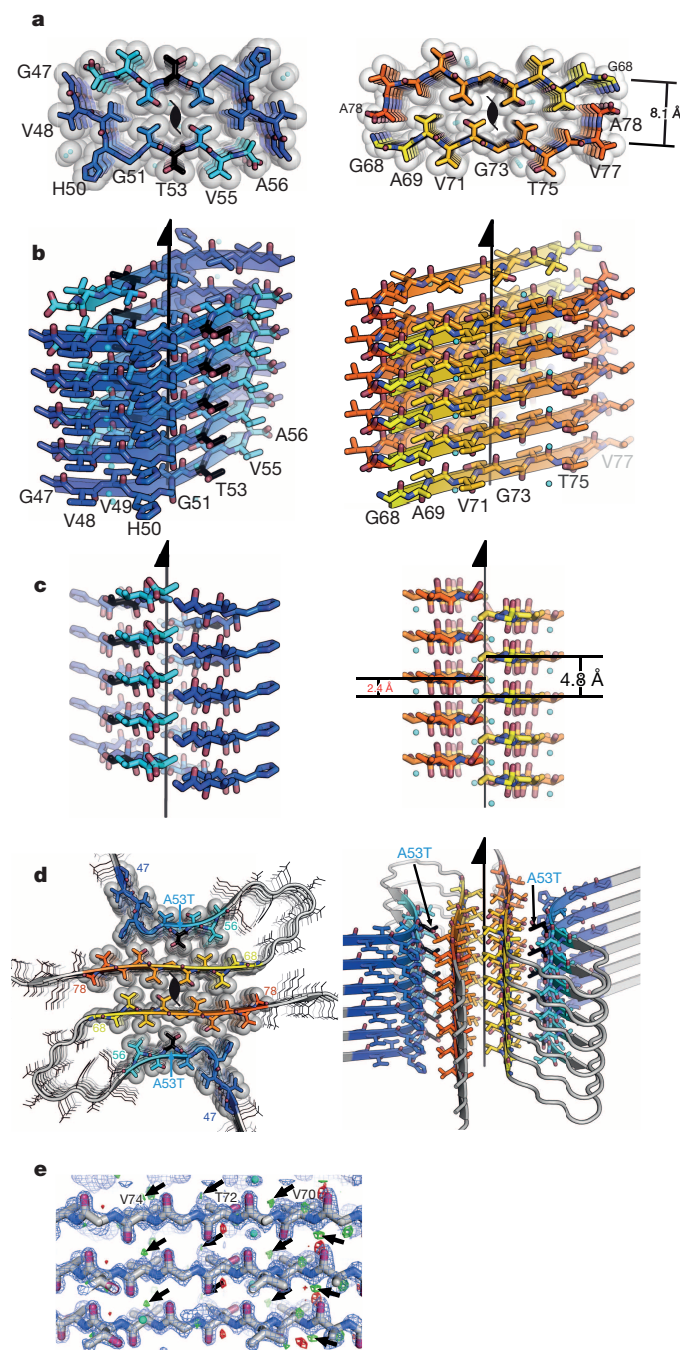
Figure 3 | Structure of the amyloid core of α-synuclein. a, The crystal structure of NACore (orange) reveals pairs of sheets as in the spines of amyloid fibrils. The A53T mutation (black) is shown in PreNAC (blue). The sheets in both structures are related by the 2_1 fibril axes shown in black. The gaps left by the interface are filled with water molecules which hydrogen-bond to the threonine residues (partially showing aqua spheres). **b, c**, Orthogonal views of the fibrillar assemblies. **d**, A speculative model of an α-synuclein protofibril containing the A53T mutation (black), where the strong interface of NACore (orange) forms the core of the fibril and its weaker interface interacts with PreNAC (blue). **e**, The locations of 5 out of a possible 73 protons are suggested by small, positive $F_o - F_c$ density (green contoured at 2.8σ, shown by arrows). The blue mesh is $2F_o - F_c$ density contoured at 1.4σ.

molecules, and several hydrogen atoms, were observed (Fig. 3e). Full models of NACore and PreNAC were refined against the MicroED data, producing structures at 1.4 Å resolution with acceptable *R* factors (Extended Data Table 1). Electron scattering factors were used in the refinement calculations[29].

NACore structure

The structure of the NACore peptide chain is a nearly fully extended β-strand (Fig. 3 and Extended Data Fig. 3). These NACore strands stack in-register into β-sheets, as had been predicted by site-directed spin labelling[16,17]. The sheets are paired (Fig. 3b), as is usual in amyloid spines, and the pairs of sheets form typical steric-zipper protofilaments (Fig. 3c), previously seen as the spines in many amyloid-like fibrils formed from short segments of fibril-forming proteins[21]. The unusual features of this steric zipper are that the 11-residue width of the zipper is longer than has been previously observed[22], and each pair of sheets contains two water molecules, each associated with a threonine side chain within the interface. Most steric zippers are completely dry. Also, in our crystals of NACore, each sheet forms two snug interfaces: interface A, with 268 Å^2 of buried accessible surface area per chain, is more extensive and presumably stronger than interface B (167 Å^2), because the terminal residues of the chains in opposing sheets bend towards each other (Fig. 3 and Extended Data Fig. 4). The structure of PreNAC reveals a peptide chain that forms a β-strand kinked at Gly51. These strands are arranged into pairs of β-sheets that, like the NACore structure, interdigitate to form steric zipper protofilaments (Fig. 3). Of special note, a five-residue segment of PreNAC ($_{51}$GVTTV$_{55}$) differs in only one residue from a five-residue segment of NACore ($_{73}$GVTAV$_{77}$), and their α-carbons superimpose closely with a root mean square deviation (r.m.s.d.) of 1.5 Å (Extended Data Fig. 4). This means that the weaker interface B of NACore mimics a hypothetical interface between NACore and PreNAC (Fig. 3d).

Relevance of NACore to Parkinson disease

The relationship of the structure of NACore to fibrils of full length α-synuclein is established by the resemblance of their diffraction patterns. Specifically, the fibre diffraction pattern of aligned fibrils of full-length and N-terminally acetylated[30] α-synuclein protein display the same principal peaks as the diffraction of aligned NACore nanocrystals (Fig. 2). All three fibrils display the strong reflection at 2.4 Å in their diffraction patterns. As seen in Fig. 3 and Extended Data Fig. 5 this reflection arises in NACore because one β-sheet of the steric zipper is translated along the fibre axis with respect to the other β-sheet by 2.4 Å, one half the 4.8 Å spacing between β-strands, permitting the two sheets to interdigitate tightly together. All three share a strong 4.6 Å reflection, which in NACore results from both the stacking of β-strands and the staggering between adjacent β-sheets of the steric zipper, while a shared reflection at near 8.2 Å probably arises from the distance between the adjacent pairs of β-sheets that make up the α-synuclein fibril (Fig. 2 and Extended Data Fig. 5). This comparison of fibre diffraction patterns (Extended Data Table 2) strongly suggests that the structure of NACore is similar to the spine of the toxic fibrils of full α-synuclein.

The combined structures of NACore and PreNAC allow us to construct a speculative model for much of the ordered segments of the A53T early-onset mutant α-synuclein (Fig. 3d). Experimental support of this model comes from the agreement of its simulated fibre diffraction with the measured diffraction patterns of α-synuclein and N-acetyl α-synuclein fibrils, as well as aligned NACore nanocrystals (Extended Data Table 2). Above we hypothesized that the weaker interface B of NACore might mimic an intramolecular interaction of PreNAC with NACore (Fig. 3). In fact, the interacting side chains in the weaker NACore interface B (G73, T75 and V77) are identical to the side chains (G51, T53, V55) interacting in the hypothetical interface of PreNAC with NACore. Assuming that this interface actually forms in fibrils of the early-onset mutant A53T, we built the model shown in Fig. 3d. The hypothetical interface of this model offers a possible reason for a greater propensity of the A53T mutant to aggregate than the wild-type sequence, conceivably leading to the early onset of PD.

The identity and structure of the cytotoxic amyloid formed by α-synuclein remains a subject of intensive research[19,31–35]. The weight
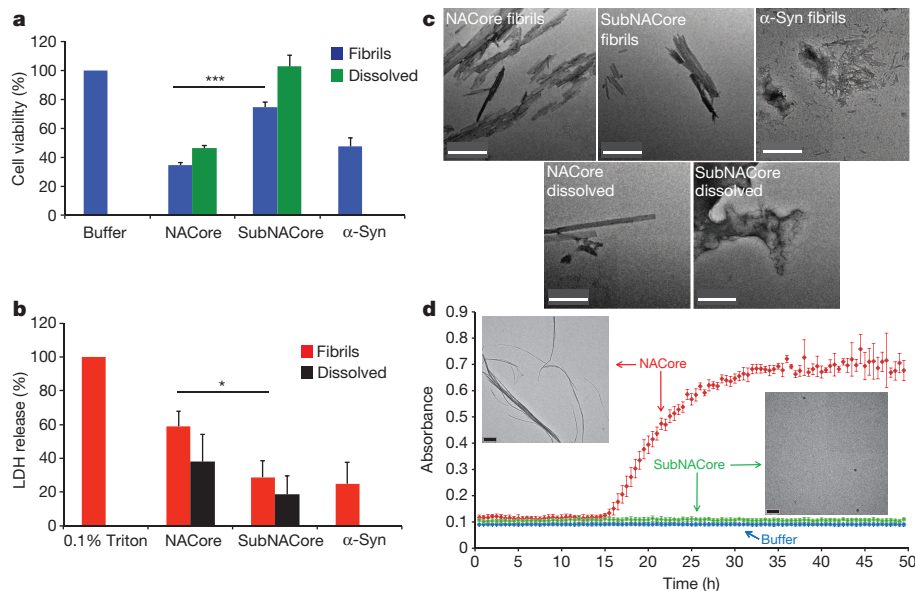
Figure 4 | NACore aggregates faster than SubNACore and is more cytotoxic to cultured cells. a, b, Cytotoxicity of NACore, SubNACore and α-synuclein measured on PC12 cells using a 3-(4,5-dimethylthiazol-2-yl)-2,5-diphenyltetrazolium bromide (MTT) assay (**a**) and a lactate dehydrogenase (LDH)-release assay (**b**). In both assays NACore is more toxic than SubNACore. Also, shaken fibrils are more toxic than an equal concentration of freshly dissolved sample. Results shown as mean ± s.e.m. based on triplicate samples. A *t*-test was used to measure statistical significance; *$P < 0.05$, ***$P < 0.001$. **c**, Representative electron micrographs of NACore, SubNACore and α-synuclein (α-syn) samples tested for cytotoxicity. NACore and α-synuclein show abundant fibrils but SubNACore shows few. NACore also forms fibrils immediately upon dissolving, whereas SubNACore shows no fibres, but instead amorphous aggregates. Scale bar, 500 nm. **d**, NACore and SubNACore were aggregated in identical conditions and monitored by turbidity. NACore begins to aggregate after 15 h while SubNACore forms no aggregates for up to 50 h. Electron microscopy of the samples at 50 h confirmed the turbidity readings (insets; scale bars, 2 μm), with error bars denoting standard deviation based on triplicate samples.

of evidence over the past decade has tilted scientific opinion from the fully developed amyloid fibrils found in Lewy bodies as the toxic entities to smaller, transient amyloid oligomers. Yet recently, quantitative arguments have been put forward in favour of fibrils[36]. Our experiments of the cytotoxicity of NACore on PC12 cells (Fig. 4) are consistent with the view that fibrils are toxic: we find that NACore shaken and aggregated for 72 h displays abundant fibrils, is more toxic than freshly dissolved NACore (Fig. 4), and is comparably toxic to similarly aggregated full α-synuclein. We also find greater cytotoxicity of NACore than SubNACore, which is shorter by two residues. This is consistent with the more rapid fibril formation of NACore than of SubNACore (Fig. 4d). These observations do not rule out the formation of a non-fibrillar, oligomeric assembly, present, but undetected, in our aggregated samples of NACore and α-synuclein. Of course, NACore is merely a fragment of full length α-synuclein, and lacks most of the membrane-binding motifs of the N terminus of the protein, which have been implicated in membrane disruption[37,38]. Yet it is clear that NACore is the minimum entity that recapitulates all the features of full length α-synuclein aggregation and toxicity.

MicroED diffraction of invisible crystals

The miniscule size of NACore crystals is typical of amyloid and also of various other biological crystals of interest. For amyloid crystals, our speculation is that the tiny size is a consequence of the natural twist of β-sheets that form the protofilaments of the fibrils. The crystal lattice restrains the twist, creating a strain in these crystals, which increases as crystals grow. Eventually this strain prevents further addition of β-strands, limiting the thickness of the needle crystals. In our experience, longer segments (for example, 11 residues compared to 9 residues) limit crystal growth even more; in the case of 11-residue NACore and 10-residue PreNAC, the strain produces nanocrystals, invisible by optical microscopy. These crystals are too small for mounting and conventional synchrotron data collection, but are ideally suited for analysis by MicroED. They are ~10^{10} times smaller

than Perutz's haemoglobin crystals and ~10^{12} times smaller than von Laue's $CuSO_4$ crystal, which yielded the first X-ray diffraction pattern. Our structures of NACore and PreNAC demonstrate that MicroED is capable of determining new and accurate structures of biological material at atomic resolutions. This finding paves the way for applications of MicroED to other biological substances of importance for which only nanocrystals can be grown. In our particular application, we have been able to learn the atomic arrangement of the core of the crucial NAC domain. This presents opportunities for structure-based design of inhibitors of amyloid formation of α-synuclein[39].

1. Spillantini, M. G. *et al.* α-Synuclein in Lewy bodies. *Nature* **388,** 839–840 (1997).
2. Goedert, M., Spillantini, M. G., Del Tredici, K. & Braak, H. 100 years of Lewy pathology. *Nature Rev. Neurol.* **9,** 13–24 (2013).
3. Polymeropoulos, M. H. *et al.* Mutation in the α-synuclein gene identified in families with Parkinson's disease. *Science* **276,** 2045–2047 (1997).
4. Krüger, R. *et al.* Ala30Pro mutation in the gene encoding α-synuclein in Parkinson's disease. *Nature Genet.* **18,** 106–108 (1998).
5. Zarranz, J. J. *et al.* The new mutation, E46K, of α-synuclein causes Parkinson and Lewy body dementia. *Ann. Neurol.* **55,** 164–173 (2004).
6. Ibáñez, P. *et al.* Causal relation between α-synuclein gene duplication and familial Parkinson's disease. *Lancet* **364,** 1169–1171 (2004).
7. Singleton, A. B. *et al.* α-Synuclein locus triplication causes Parkinson's disease. *Science* **302,** 841 (2003).
8. Uéda, K. *et al.* Molecular cloning of cDNA encoding an unrecognized component of amyloid in Alzheimer disease. *Proc. Natl Acad. Sci. USA* **90,** 11282–11286 (1993).
9. Biere, A. L. *et al.* Parkinson's disease-associated α-synuclein is more fibrillogenic than β- and γ-synuclein and cannot cross-seed its homologs. *J. Biol. Chem.* **275,** 34574–34579 (2000).
10. Giasson, B. I., Murray, l. V. J., Trojanowski, J. Q. & Lee, V. M.-Y. A hydrophobic stretch of 12 amino acid residues in the middle of α-synuclein is essential for filament assembly. *J. Biol. Chem.* **276,** 2380–2386 (2001).
11. Du, H.-N. *et al.* A peptide motif consisting of glycine, alanine, and valine is required for the fibrillization and cytotoxicity of human α-synuclein. *Biochemistry* **42,** 8870–8878 (2003).

12. Periquet, M., Fulga, T., Myllykangas, L., Schlossmacher, M. G. & Feany, M. B. Aggregated α-synuclein mediates dopaminergic neurotoxicity *in vivo*. *J. Neurosci.* **27,** 3338–3346 (2007).
13. Han, H., Weinreb, P. H. & Lansbury, P. T. The core Alzheimer's peptide NAC forms amyloid fibrils, which seed and are seeded by β-amyloid: is NAC a common trigger or target in neurodegenerative disease? *Chem. Biol.* **2,** 163–169 (1995).
14. El-Agnaf, O. M. *et al.* Aggregates from mutant and wild-type α-synuclein proteins and NAC peptide induce apoptotic cell death in human neuroblastoma cells by formation of β-sheet and amyloid-like filaments. *FEBS Lett.* **440,** 71–75 (1998).
15. Crowther, R. A., Daniel, S. E. & Goedert, M. Characterisation of isolated α-synuclein filaments from substantia nigra of Parkinson's disease brain. *Neurosci. Lett.* **292,** 128–130 (2000).
16. Der-Sarkissian, A., Jao, C. C., Chen, J. & Langen, R. Structural organization of α-synuclein fibrils studied by site-directed spin labeling. *J. Biol. Chem.* **278,** 37530–37535 (2003).
17. Chen, M., Margittai, M., Chen, J. & Langen, R. Investigation of α-synuclein fibril structure by site-directed spin labeling. *J. Biol. Chem.* **282,** 24970–24979 (2007).
18. Miake, H., Mizusawa, H., Iwatsubo, T. & Hasegawa, M. Biochemical characterization of the core structure of α-synuclein filaments. *J. Biol. Chem.* **277,** 19213–19219 (2002).
19. Conway, K. A., Harper, J. D. & Lansbury, P. T. Accelerated *in vitro* fibril formation by a mutant α-synuclein linked to early-onset Parkinson disease. *Nature Med.* **4,** 1318–1320 (1998).
20. Polymeropoulos, M. H. *et al.* Mutation in the α-synuclein gene identified in families with Parkinson's disease. *Science* **276,** 2045–2047 (1997).
21. Nelson, R. *et al.* Structure of the cross-β spine of amyloid-like fibrils. *Nature* **435,** 773–778 (2005).
22. Sawaya, M. R. *et al.* Atomic structures of amyloid cross-β spines reveal varied steric zippers. *Nature* **447,** 453–457 (2007).
23. Bodles, A. M., Guthrie, D. J., Greer, B. & Irvine, G. B. Identification of the region of non-Aβ component (NAC) of Alzheimer's disease amyloid responsible for its aggregation and toxicity. *J. Neurochem.* **78,** 384–395 (2001).
24. Nannenga, B. L. & Gonen, T. Protein structure determination by MicroED. *Curr. Opin. Struct. Biol.* **27,** 24–31 (2014).
25. Nannenga, B. L., Shi, D., Leslie, A. G. W. & Gonen, T. High-resolution structure determination by continuous-rotation data collection in MicroED. *Nature Methods* **11,** 927–930 (2014).
26. Shi, D., Nannenga, B. L., Iadanza, M. G. & Gonen, T. Three-dimensional electron crystallography of protein microcrystals. *eLife* **2,** e01345 (2013).
27. Nannenga, B. L., Shi, D., Hattne, J., Reyes, F. E. & Gonen, T. Structure of catalase determined by MicroED. *eLife* **3,** e03600 (2014).
28. Yonekura, K., Kato, K., Ogasawara, M., Tomita, M. & Toyoshima, C. Electron crystallography of ultrathin 3D protein crystals: atomic model with charges. *Proc. Natl Acad. Sci. USA* **112,** 3368–3373 (2015).
29. Doyle, P. A. & Turner, P. S. Relativistic Hartree–Fock X-ray and electron scattering factors. *Acta Crystallogr. A* **24,** 390–397 (1968).
30. Sarafian, T. A. *et al.* Impairment of mitochondria in adult mouse brain overexpressing predominantly full-length, N-terminally acetylated human α-synuclein. *PLoS ONE* **8,** e63557 (2013).
31. Caughey, B. & Lansbury, P. T. Protofibrils, pores, fibrils, and neurodegeneration: separating the responsible protein aggregates from the innocent bystanders. *Annu. Rev. Neurosci.* **26,** 267–298 (2003).
32. Danzer, K. M., Schnack, C., Sutcliffe, A., Hengerer, B. & Gillardon, F. Functional protein kinase arrays reveal inhibition of p-21-activated kinase 4 by α-synuclein oligomers. *J. Neurochem.* **103,** 2401–2407 (2007).
33. Karpinar, D. P. *et al.* Pre-fibrillar α-synuclein variants with impaired β-structure increase neurotoxicity in Parkinson's disease models. *EMBO J.* **28,** 3256–3268 (2009).
34. Winner, B. *et al.* *In vivo* demonstration that α-synuclein oligomers are toxic. *Proc. Natl Acad. Sci. USA* **108,** 4194–4199 (2011).
35. Chen, S. W. *et al.* Structural characterization of toxic oligomers that are kinetically trapped during α-synuclein fibril formation. *Proc. Natl Acad. Sci. USA* **112,** E1994–E2003 (2015).
36. Bousset, L. *et al.* Structural and functional characterization of two α-synuclein strains. *Nature Commun.* **4,** 2575 (2013).
37. Auluck, P. K., Caraveo, G. & Lindquist, S. α-Synuclein: membrane interactions and toxicity in Parkinson's disease. *Annu. Rev. Cell Dev. Biol.* **26,** 211–233 (2010).
38. Lee, J. C., Langen, R., Hummel, P. A., Gray, H. B. & Winkler, J. R. α-Synuclein structures from fluorescence energy-transfer kinetics: implications for the role of the protein in Parkinson's disease. *Proc. Natl Acad. Sci. USA* **101,** 16466–16471 (2004).
39. Sievers, S. A. *et al.* Structure-based design of non-natural amino-acid inhibitors of amyloid fibril formation. *Nature* **475,** 96–100 (2011).
40. Comellas, G. *et al.* Structured regions of α-synuclein fibrils include the early-onset Parkinson's disease mutation sites. *J. Mol. Biol.* **411,** 881–895 (2011).
41. Vilar, M. *et al.* The fold of α-synuclein fibrils. *Proc. Natl Acad. Sci. USA* **105,** 8637–8642 (2008).
42. Goldschmidt, L., Teng, P. K., Riek, R. & Eisenberg, D. Identifying the amylome, proteins capable of forming amyloid-like fibrils. *Proc. Natl Acad. Sci. USA* **107,** 3487–3492 (2010).

Author Contributions M.I.I. characterized the α-synuclein segments and crystals. M.I.I. and S.S. conducted the toxicity assays. L.M.J. synthesized and purified NACore peptide. M.A.A. prepared the N-terminally acetylated α-synuclein. S.S. and M.Z. prepared wild-type α-synuclein. J.W. performed the mass spectrometry analyses of α-synuclein. M.I.I. and L.M.J. crystallized NACore. E.G. grew crystals of SubNACore. E.G., M.I.I. and M.R.S. collected and processed the data and solved the structure of SubNACore. L.J. and J.A.R. identified and crystallized PreNAC. J.A.R., D.S., B.L.N. and T.G. collected MicroED data on PreNAC and NACore nanocrystals. J.A.R., F.E.R., J.H., T.G., L.J., M.R.S., and D.C. processed the MicroED data and solved the structure of PreNAC and NACore. J.A.R., M.R.S., D.C., M.M. and S.B. collected XFEL diffraction from NACore nanocrystals. A.S.B. and N.K.S. processed the XFEL data. M.R.S and L.J. built the structure model of A53T α-synuclein protofibril. J.A.R., M.I.I., M.R.S., D.C., S.S. and E.G. prepared the figures. J.A.R., M.I.I., M.R.S., D.C., T.G. and D.S.E. wrote the paper, and all authors commented on the paper.

Author Information Atomic coordinates and structure factors have been deposited in the Protein Data Bank under accession codes 4RIK (SubNACore), 4RIL (NACore) and 4ZNN (PreNAC). The maps for PreNAC and NACore have been deposited in the EMDB with accession codes EMD-3001 and EMD-3028, respectively. Reprints and permissions information is available at www.nature.com/reprints. The authors declare no competing financial interests. Readers are welcome to comment on the online version of the paper. Correspondence and requests for materials should be addressed to D.S.E. (david@mbi.ucla.edu) and T.G. (gonent@janelia.hhmi.org).

METHODS

Data reporting. No statistical methods were used to predetermine sample size. The experiments were not randomized. The investigators were not blinded to allocation during experiments and outcome assessment.

Crystallization. Microcrystals of SubNACore ($_{69}$AVVTGVTAV$_{77}$) were grown from synthetic peptide purchased from CS Bio. Crystals were grown at room temperature by hanging drop vaporization. Lyophilized peptide was dissolved in water at 2.9 mg ml^{-1} concentration in 48 mM lithium hydroxide. Peptide was mixed in a 2:1 ratio with reservoir containing 0.9 M ammonium phosphate, and 0.1 M sodium acetate pH 4.6.

Nanocrystals of NACore, $_{68}$GAVVTGVTAV$_{78}$, were grown from synthetic peptide purchased from CS Bio. Ten batches of synthesized peptide (CSBio) at a concentration of 1 mg ml^{-1} in sterile water were shaken at 37 °C on a Torrey Pines orbital mixing plate at speed setting 9, overnight. The insoluble material was washed in 30% (w/v) glycerol then stored in water at room temperature before diffraction. The sample contained a mixture of fibrils and crystals.

Nanocrystals of PreNAC ($_{47}$GVVHGVTTVA$_{56}$) were grown from synthetic peptide purchased from InnoPep. Crystallization trials of synthesized peptide were prepared in batch. Peptide was weighed and dissolved in sterile-filtered 50 mM phosphate buffer pH 7.0 with 0.1% DMSO at a concentration of 5 mg ml^{-1}. This solution was shaken at 37 °C on a Torrey Pines orbital mixing plate at speed setting 9, overnight.

Data collection and processing. X-ray diffraction data from microcrystals of SubNACore were collected using synchrotron radiation at the Advanced Photon Source, Northeast Collaborative Access Team micro focus beam line 24-ID-E. The beam line was equipped with an ADSC Quantum 315 CCD detector. Data from a single crystal were collected in 5° wedges at a wavelength of 0.9791 Å using a 5 μm beam diameter. We used data from three different sections along the needle axis. The crystals were cryo-cooled (100 K) for data collection. Data were processed and reduced using Denzo/Scalepack from the HKL suite of programs[43].

Electron diffraction data from nanocrystals of NACore and PreNAC were collected using MicroED techniques[25,26]. These nanocrystals typically clump together. To break up the clumps, an approximately 100 μl volume of nanocrystals was placed in a sonication bath for 30 min. Nanocrystals were deposited onto a Quantifoil holey-carbon EM grid in a 2–3 μl drop after appropriate dilution, which optimized for crystal density on the grid. All grids were then blotted and vitrified by plunging into liquid ethane using a Vitrobot Mark IV (FEI), then transferring to liquid nitrogen for storage. Frozen hydrated grids were transferred to a cryo-TEM using a Gatan 626 cryo-holder. Diffraction patterns and crystal images were collected using an FEG-equipped FEI Tecnai F20 TEM operating at 200 kV and recorded using a bottom mount TVIPS F416 CMOS camera with a sensor size of 4,096 × 4,096 pixels, each 15.6 × 15.6 μm. Diffraction patterns were recorded by operating the detector in rolling shutter mode with 2 × 2 pixel binning, producing a final image 2,048 × 2,048 pixels in size. Individual image frames were taken with exposure times of 3–4 s per image, using a selected area aperture with an illuminating spot size of approximately 1 μm. This geometry equates to an electron dose of less than 0.1 e$^-$ per Å^2 per second. During each exposure, crystals were continuously rotated within the beam at a rate of 0.3° per second, corresponding to 1.2° wedge per frame. Diffraction data were collected from several crystals each oriented differently with respect to the rotation axis. These data sets each spanned wedges of reciprocal space ranging from 40° to 80°.

X-ray diffraction data from nanocrystals of NACore were collected using XFEL radiation at the CXI instrument (Coherent X-ray Imaging) at the Linear Coherent Light Source (LCLS)-SLAC. The photon energy of the X-ray pulses was 8.52 keV (1.45 Å). Each 40 fs pulse contained up to 6 × 10^{11} photons at the sample position, taking into account a beam line transmission of 60%. The diameter of the beam was approximately 1 μm. We used a concentration of approximately 25 μl of pelleted material suspended in 1 ml water. The sample was injected into the XFEL beam using a liquid jet injector and a gas dynamic virtual nozzle[44]. The micro jet width was approximately 4 μm and the flow rate was 40 μl min^{-1}. The sample caused noticeable sputtering of the liquid jet. XFEL data were processed using cctbx.xfel[45,46].

Calibration of the sample to detector distance in MicroED was accomplished using a polycrystalline gold standard and by referencing the prominent reflections in the electron diffraction experiment with the corresponding reflections in the XFEL data. Calibration of the x/y locations of the 64-tile CSPAD detector was performed by cctbx.xfel by refining the optically measured tile positions against a thermolysin data set[45].

To gain compatibility with conventional X-ray data processing programs, the MicroED diffraction images were converted from tiff or TVIPS format to the SMV crystallographic format. We used XDS to index the diffraction images[47], and XSCALE for merging and scaling together data sets originating from different

crystals. For NACore, data from four crystals were merged, while for PreNAC, data from three crystals were merged to assemble the final data sets (see Extended Data Table 1).

Structure determination. The molecular replacement solution for SubNACore was obtained using the program Phaser[48]. The search model consisted of a geometrically ideal β-strand composed of nine alanine residues. Crystallographic refinements were performed with the program Refmac[49].

The molecular replacement solution for NACore was obtained using the program Phaser[48]. The search model consisted of the SubNACore structure determined previously. Crystallographic refinements were performed with the program Phenix[50] and Buster[51].

The molecular replacement solution for PreNAC was obtained using the program Phaser[48]. The search model consisted of a geometrically ideal β-strand composed of six residues with sequence GVTTVA. Crystallographic refinements were performed with the program Phenix[50] and Refmac[49].

Model building for all segments was performed using COOT[52]. Data processing and refinement statistics are reported in Extended Data Table 1. The coordinates of the final models and the structure factors have been deposited in the Protein Data Bank with PDB code 4RIK for SubNACore, 4RIL for NACore, and 4ZNN for PreNAC. The structures were illustrated using Pymol[53].

Protein expression and purification. The human wild-type α-synuclein construct has been previously characterized[54] (pRK172, ampicillin, T7 promoter) with sequence: MDVFMKGLSKAKEGVVAAAEKTKQGVAEAAGKTKEGVL YVGSKTKEGVVHGVATVAEKTKEQVTNVGGAVVTGVTAVAQKTVEGAG SIAAATGFVKKDQLGKNEEGAPQEGILEDMPVDPDNEAYEMPSEEGYQDY EPEA.

Full length α-synuclein was purified according to published protocols[34]. The α-synuclein construct was transformed into *Escherichia coli* expression cell line BL21 (DE3) gold (Agilent Technologies) for wild-type α-synuclein protein expression. A single colony was incubated into 100 ml LB Miller broth (Fisher Scientific) supplemented with 100 μg ml^{-1} ampicillin (Fisher Scientific) and grown overnight at 37 °C. One litre of LB (Miller) supplemented with 100 μg ml^{-1} ampicillin in 2-l shaker flasks was incubated with 10 ml of overnight culture and grown at 37 °C until the culture reached OD$_{600}$ ≈ 0.6–0.8 as measured by a BioPhotometer UV/VIS Photometer (Eppendorf). IPTG (Isopropyl β-D-1-thiogalactopyranoside) was added to a final concentration of 0.5 mM, and grown for 4–6 h at 30 °C. Cells were harvested by centrifugation at 5,500g for 10 min at 4 °C. The cell pellet was frozen and stored at −80 °C.

The cell pellet was thawed on ice and resuspended in lysis buffer (100 mM Tris-HCl pH 8.0, 500 mM NaCl, 1 mM EDTA pH 8.0) and lysed by sonication. Crude cell lysate was clarified by centrifugation at 15,000g for 30 min at 4 °C. The clarified cell lysate was boiled and cell debris was removed by centrifugation. Protein in the supernatant was precipitated in acid at pH 3.5 through addition of HCl by titration to protein solution on ice while stirring then centrifuged for an additional 15,000g for 30 min at 4 °C. Supernatant was dialysed against buffer A (20 mM Tris-HCl, pH 8.0). After dialysis the solution was filtered through a 0.45 μm syringe (Corning) before loading onto a 20 ml HiPrep Q HP 16/10 column (GE Healthcare). The Q-HP column was washed with five column volumes of buffer A and protein eluted using a linear gradient to 100% in five column volumes of buffer B (20 mM Tris-HCl, 1 M NaCl, pH 8.0). Protein eluted at around 50–70% buffer B; peak fractions were pooled. Pooled samples were concentrated approximately tenfold using Amicon Ultra-15 centrifugal filters. Approximately 5 ml of the concentrated sample was loaded onto a HiPrep 26/60 Sephacryl S-75 HR column equilibrated with filtration buffer (25 mM sodium phosphate, 100 mM NaCl, pH 7.5). Peak fractions were pooled from the gel filtration column and dialysed against 5 mM Tris-HCl, pH 7.5, concentrated to 3 mg ml^{-1}. These were filtered through a 0.2 μm pore size filter (Corning) and stored at 4 °C.

Recombinantly expressed full-length α-synuclein with an N-terminal acetylation was prepared and purified in the following way based on a protocol detailed in ref. 16 The α-synuclein plasmid was co-expressed with a heterodimeric protein acetylation complex from *Schizosaccharomyces pombe* to acetylate the N terminus (pACYC-DUET, chloramphenicol, T7 promoter)[55]. The two vectors were co-transformed into *E. coli* BL21 (DE3) using media containing both ampicillin and chloramphenicol. Cell cultures were grown in TB media containing ampicillin and chloramphenicol and induced to express α-synuclein with 0.5 mM IPTG overnight at 25 °C. Cells were harvested by centrifugation, the cell pellet then resuspended in lysis buffer (100 mM Tris-HCl pH 8.0, 500 mM NaCl, 1 mM EDTA pH 8.0, and 1 mM phenylmethylsulfonyl fluoride) and cells lysed using an Emulsiflex homogenizer (Avestin). The lysate was boiled and debris removed by centrifugation. A protein fraction was also removed by precipitation at low pH on ice followed by centrifugation. The remaining supernatant was pH adjusted by titration and dialysed against buffer A (20 mM Tris-HCl, pH 8.0,

1 mM DTT, 1 mM EDTA, pH 8.0). The resulting protein solution was loaded onto a 5 ml Q-Sepharose FF column (GE Healthcare) equilibrated with buffer A and eluted against a linear gradient of buffer B (1 M NaCl, 20 mM Tris-HCl, pH 8.0, 1 mM DTT, 1 mM EDTA, pH 8.0). Fractions containing α-synuclein were identified using SDS–PAGE, collected, concentrated and further purified by size exclusion (Sephacryl S-100 16/60, GE Healthcare) in 20 mM Tris, pH 8.0, 100 mM NaCl, 1 mM DTT, 1 mM EDTA. Purity of fractions was assessed by SDS–PAGE.

Acetylated protein was characterized by LC–MS[30,56]. Expected average mass: 14460.1 Da for α-synuclein and 14502.1 Da for acetylated α-synuclein. Observed average mass: 14464.0 Da for α-synuclein and 14506.0 Da for acetylated α-synuclein (Extended Data Fig. 6). The shift of 4 Da between observed and expected average masses is due to instrumental error.

Fibril formation and detection. Purified α-synuclein in 50 mM Tris, 150 mM KCl, pH 7.5 was shaken at a concentration of 500 μM at 37 °C in a Torey Pine shaker. To form the fibrillar samples of SubNACore and NACore, lyophilized peptides were dissolved to a final concentration of 500 μM in 5 mM lithium hydroxide, 20 mM sodium phosphate pH 7.5 and 0.1 M NaCl. All samples were shaken at 37 °C in a Torey Pine shaker for 72 h. Freshly dissolved samples were prepared by dissolving lyophilized peptides immediately before addition to cells for assays.

Turbidity measurements were used to compare NACore and SubNACore aggregation. Peptide samples were freshly dissolved to 1.6 mM in a sample buffer with 5 mM LiOH and 1% DMSO and then filtered through a PVDF filter (Millipore, 0.1 μm). Measurements were performed using a black NUNC 96 well plate with 200 μl of sample per well (3–4 replicates per sample). The plate was agitated at 37 °C, with a 3 mm rotation diameter, at 300 r.p.m. in a Varioskan microplate reader (Thermo). Absorbance readings were recorded every 3–15 min at 340 nm.

Negative-stain transmission electron microscopy. Cytotoxicity samples were evaluated for presence of fibrils by electron microscopy. In brief, 5-μl samples were spotted directly on freshly glow-discharged carbon-coated electron microscopy grids (Ted Pella). After 4 min incubation, grids were rinsed twice with 5 μl distilled water and stained with 2% uranyl acetate for 1 min. Specimens were examined on an FEI T12 electron microscope.

Fibril diffraction. Fibrils formed from purified α-synuclein with and without N-terminal acetylation were concentrated by centrifugation, washed, and oriented while drying between two glass capillaries. Likewise, NACore nanocrystals were also concentrated, washed with nanopure water, and allowed to orient while drying between two glass capillaries. The glass capillaries holding the aligned fibrils or nanocrystals were mounted on a brass pin for diffraction at room temperature using 1.54 Å X-rays produced by a Rigaku FRE+ rotating anode generator equipped with an HTC imaging plate. All patterns were collected at a distance of 180 mm and analysed using the Adxv software package[57]. A simulated pattern from the full length α-synuclein model presented in Fig. 3 was obtained by calculating structure factors from the model using the sfall module from CCP4, assigning the model a unit cell of 200 × 4.74 × 200 Å. Cylindrical averaging of these structure factors about the fibre axis (y axis) direction produced a set of simulated fibril diffraction intensities.

Cytotoxicity assays. Adherent PC12 cells (ATCC CRL-1721) were cultured in ATCC-formulated RPMI-1640 medium (ATCC 30-2001) supplemented with 10% horse serum and 5% fetal bovine serum and plated at 10,000 cells per well to a final volume of 90 μl. All MTT assays were performed with Cell Titer 96 aqueous non-radioactive cell proliferation kit (MTT, Promega cat. no. 4100). Cells were cultured in 96-well plates for 20 h at 37 °C in 5% CO₂ before addition of samples (Costar cat. no. 3596). 10 μl of sample was added to each well containing 90 μl of medium and incubated for 24 h at 37 °C in 5% CO₂. Then, 15 μl dye solution (Promega cat. no. 4102) was added into each well, followed by incubation for 4 h at 37 °C in 5% CO₂. This was followed by the addition of 100 μl solubilization Solution/Stop Mix (Promega cat. no. 4101) to each well. After 12 h incubation at room temperature, the absorbance was measured at 570 nm. Background absorbance was recorded at 700 nm. The data was normalized with cells treated with 1% (w/v) SDS to 0% reduction, and cells treated with sample buffer to 100% reduction.

Lactose dehydrogenase assays were done using CytoTox-ONE Homogeneous Membrane Integrity, (Promega, cat. no. G7890) as per manufacturer's instructions.

In brief, cells were plated in 96-well, black-wall, clear-bottom (Fisher cat. no. 07-200-588) tissue culture plates at 10,000 cells per well to a final volume of 90 μl. Cells were incubated for an additional 20 h at 37 °C in 5% CO₂ before addition of samples. Next, 10 μl of sample was added to each well, following which the cells were incubated for another 24 h. 100 μl of reagent was added to each well and incubated for 15 min at room temperature. The addition of 50 μl of stop solution stopped the reaction. Fluorescence was measured in a Spectramax M5 (Molecular Devices) using excitation and emission wavelengths of 560 nm and 590 nm, respectively. Data was normalized using cells treated with buffer as 0% release and 0.1% Triton X-100 as 100% release.

Construction of α-synuclein A53T fibril model. A model for full-length α-synuclein A53T mutant fibrils that are involved in the early onset of PD was constructed using a section of the NACore crystal packing as a scaffold. Figure 3 illustrates the four copies of the NACore segment used for the scaffold. The crystal structure of the two inner strands was adapted with minimal changes as the analogous segments 68–78. The structure of PreNAC was matched onto the weak interface of the NACore structure. Only 4 of the 11 side chains in the segment 46–56 differ from those in the NACore segment 68–78 and residues V51–V55 can be closely matched to V71–V75. Hence the model for both the homotypic interface and heterotypic interface in the full-length fibre model closely resemble those observed in the NACore structure. The regions outside these segments were adapted from the structure of the native α-synuclein fold, PDB ID: 2KKW[58]. These segments were spliced in manually using COOT. The models were energy minimized and temperature annealed using the program CNS[59] with hydrogen-bonding potential[60]. The simulated fibre diffraction pattern calculated from this model shows prominent reflections that agree with those observed in fibre diffraction patterns of NACore, α-synuclein, and N-acetyl α-synuclein (Extended Data Table 2).

43. Otwinowski, Z. & Minor, W. in *Methods in Enzymology* (eds Carter, C. W. Jr & Sweet, R. M.) Vol. 276 307–326 (Academic Press, 1997).
44. Weierstall, U., Spence, J. C. H. & Doak, R. B. Injector for scattering measurements on fully solvated biospecies. *Rev. Sci. Instrum.* **83**, 035108 (2012).
45. Hattne, J. *et al.* Accurate macromolecular structures using minimal measurements from X-ray free-electron lasers. *Nature Methods* **11**, 545–548 (2014).
46. Sauter, N. K., Hattne, J., Grosse-Kunstleve, R. W. & Echols, N. New Python-based methods for data processing. *Acta Crystallogr. D* **69**, 1274–1282 (2013).
47. Kabsch, W. XDS. *Acta Crystallogr. D* **66**, 125–132 (2010).
48. McCoy, A. J. *et al.* Phaser crystallographic software. *J. Appl. Crystallogr.* **40**, 658–674 (2007).
49. Murshudov, G. N., Vagin, A. A. & Dodson, E. J. Refinement of macromolecular structures by the maximum-likelihood method. *Acta Crystallogr. D* **53**, 240–255 (1997).
50. Afonine, P. V. *et al.* Towards automated crystallographic structure refinement with phenix.refine. *Acta Crystallogr. D* **68**, 352–367 (2012).
51. Blanc, E. *et al.* Refinement of severely incomplete structures with maximum likelihood in BUSTER-TNT. *Acta Crystallogr. D* **60**, 2210–2221 (2004).
52. Emsley, P., Lohkamp, B., Scott, W. G. & Cowtan, K. Features and development of Coot. *Acta Crystallogr. D* **66**, 486–501 (2010).
53. Delano, W. *The PyMOL Molecular Graphics System* (Schrödinger LLC) http://www.pymol.org.
54. Jakes, R., Spillantini, M. G. & Goedert, M. Identification of two distinct synucleins from human brain. *FEBS Lett.* **345**, 27–32 (1994).
55. Johnson, M., Coulton, A. T., Geeves, M. A. & Mulvihill, D. P. Targeted amino-terminal acetylation of recombinant proteins in E. coli. *PLoS ONE* **5**, e15801 (2010).
56. Whitelegge, J. P., Zhang, H., Aguilera, R., Taylor, R. M. & Cramer, W. A. Full subunit coverage liquid chromatography electrospray ionization mass spectrometry (LCMS+) of an oligomeric membrane protein: cytochrome *b₆f* complex from spinach and the cyanobacterium *Mastigocladus laminosus*. *Mol. Cell. Proteomics MCP* **1**, 816–827 (2002).
57. Arvai, A. *Adxv - A Program to Display X-ray Diffraction Images* (2015).
58. Rao, J. N., Jao, C. C., Hegde, B. G., Langen, R. & Ulmer, T. S. A combinatorial NMR and EPR approach for evaluating the structural ensemble of partially folded proteins. *J. Am. Chem. Soc.* **132**, 8657–8668 (2010).
59. Brunger, A. T. Version 1.2 of the crystallography and NMR system. *Nature Protocols* **2**, 2728–2733 (2007).
60. Fabiola, F., Bertram, R., Korostelev, A. & Chapman, M. S. An improved hydrogen bond potential: impact on medium resolution protein structures. *Protein Sci.* **11**, 1415–1423 (2002).
61. Read, R. J. Improved Fourier coefficients for maps using phases from partial structures with errors. *Acta Crystallogr. A* **42**, 140–149 (1986).
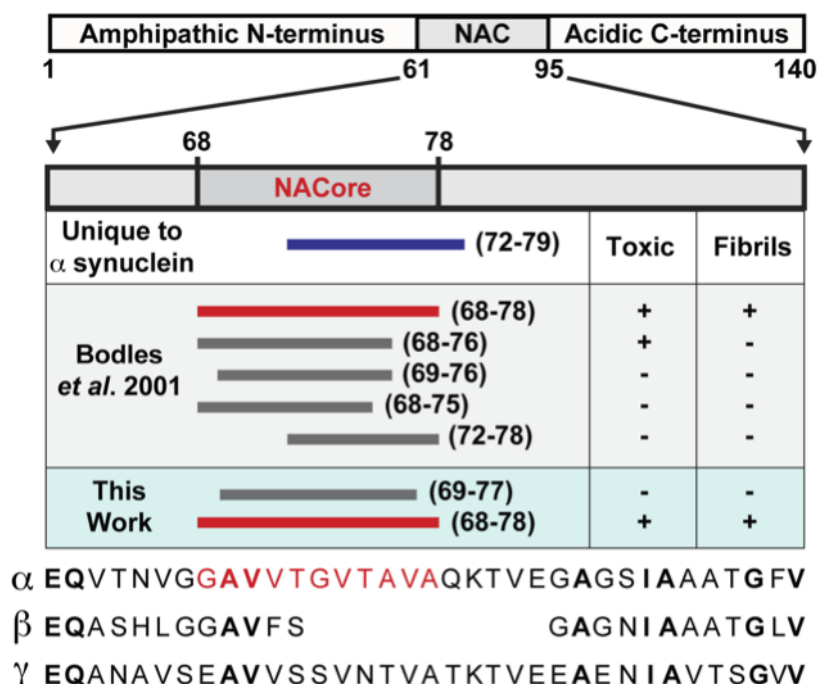
Extended Data Figure 1 | A schematic representation of α-synuclein, highlighting the NAC region (residues 61–95) and within it the NACore sequence (residues 68–78). A series of bars span regions of α-synuclein that are of interest to this work. Among the three synuclein paralogues (α, β and γ), the region whose sequence is unique to α-synuclein is shown as a blue bar (residues 72–83) that overlaps with a large portion of NACore. Segments investigated in ref. 23 are also shown. These span a variety of regions within NACore. Two of the segments we investigate here, SubNACore and NACore, are shown in this context. Only one of the segments studied ref. 23 is an exact match to our NACore sequence, and only this segment is both toxic and fibrillar. The sequences of α-synuclein, β-synuclein, and γ-synuclein are shown as a reference with conserved residues in bold and the NACore sequence in red.
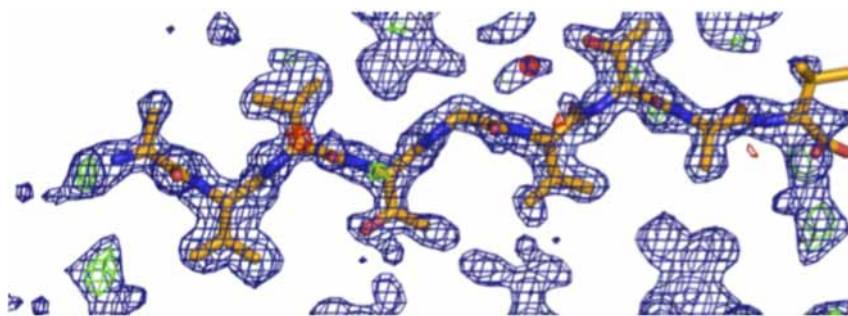
Extended Data Figure 2 | NACore difference density maps calculated after successful molecular replacement using the SubNACore search model clearly revealed the positions of the missing residues (positive $F_o - F_c$ density at N and C termini corresponding to G68 and A78) and one water molecule near a threonine side chain (red circle); a second water was located during the refinement process. The blue mesh represents $2F_o - F_c$ density contoured at 1.2σ. The green and red mesh represent $F_o - F_c$ densities contoured at 3.0 and -3.0σ, respectively. All maps were σ_A-weighted[61].
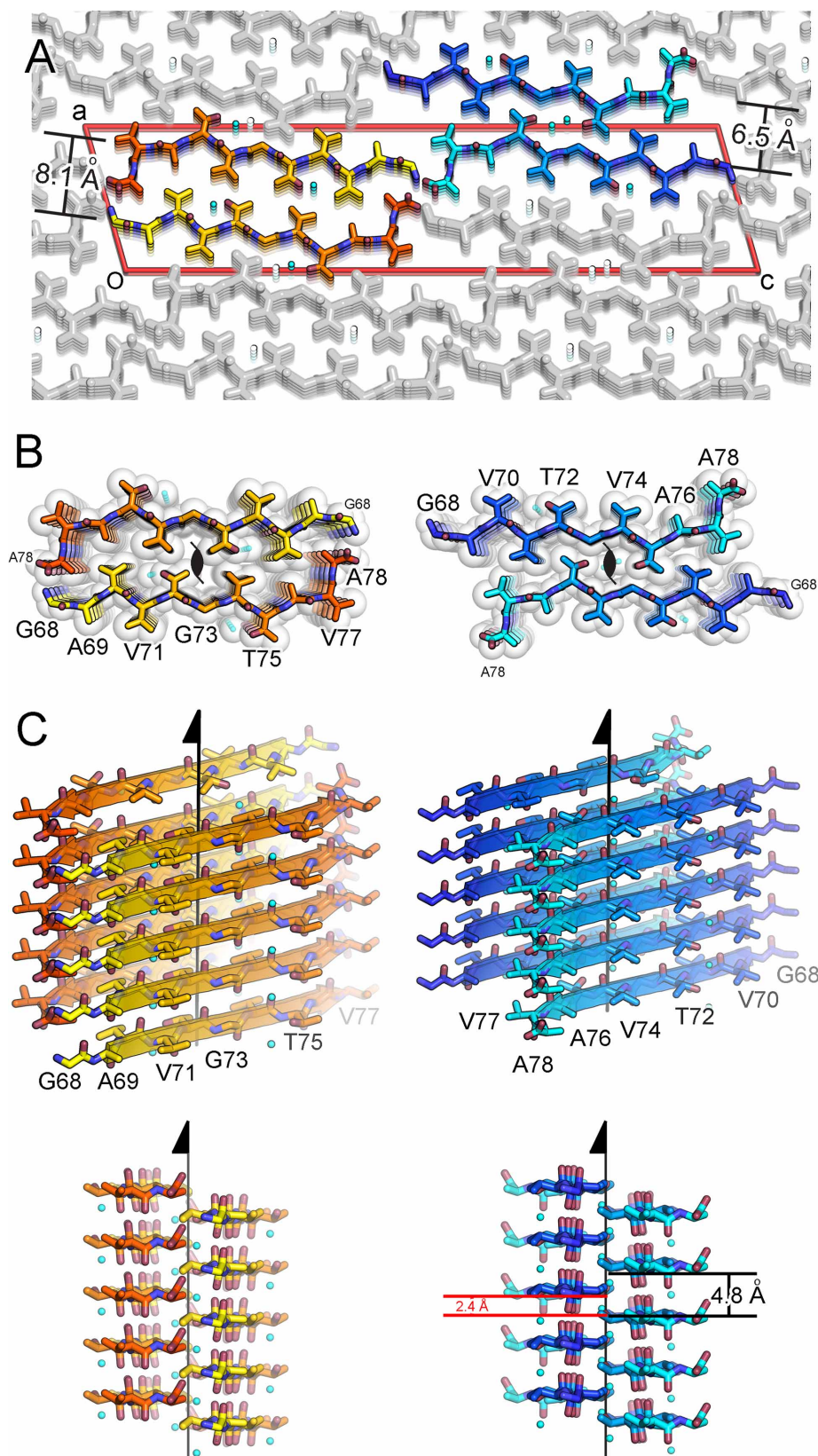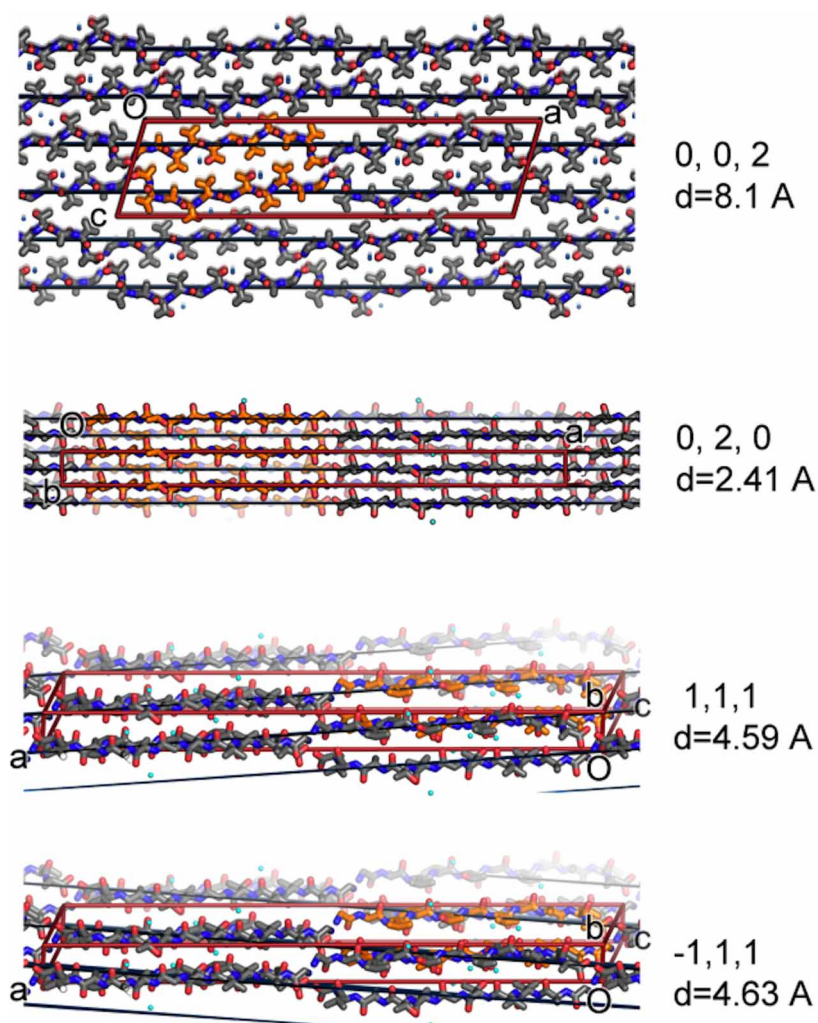
Extended Data Figure 3 | The crystal structure of NACore reveals pairs of sheets as in the spines of amyloid fibrils. a, NACore's two types of sheet–sheet interfaces: a larger interface (orange, 268 Å² of buried accessible surface area per chain) we call interface A, and a weaker interface (blue, 167 Å²) we call interface B. The crystal is viewed along the hydrogen-bonding direction (crystal 'b' dimension). The red lines outline the unit cell. **b,** The van der Waals packing between sheets. The sheets are related by a 2_1 screw axis denoted in black. The only gaps left by the interface are filled with water molecules which hydrogen-bond to the threonine residues (partially showing aqua spheres). The shape complementarity of both interfaces is 0.7. The viewing direction is the same as in **a**. **c,** Orthogonal view of the fibrillar assembly. The protofibril axis, coinciding with the 2_1 screw axis designated by the arrow, runs vertically between the pairs of sheets.
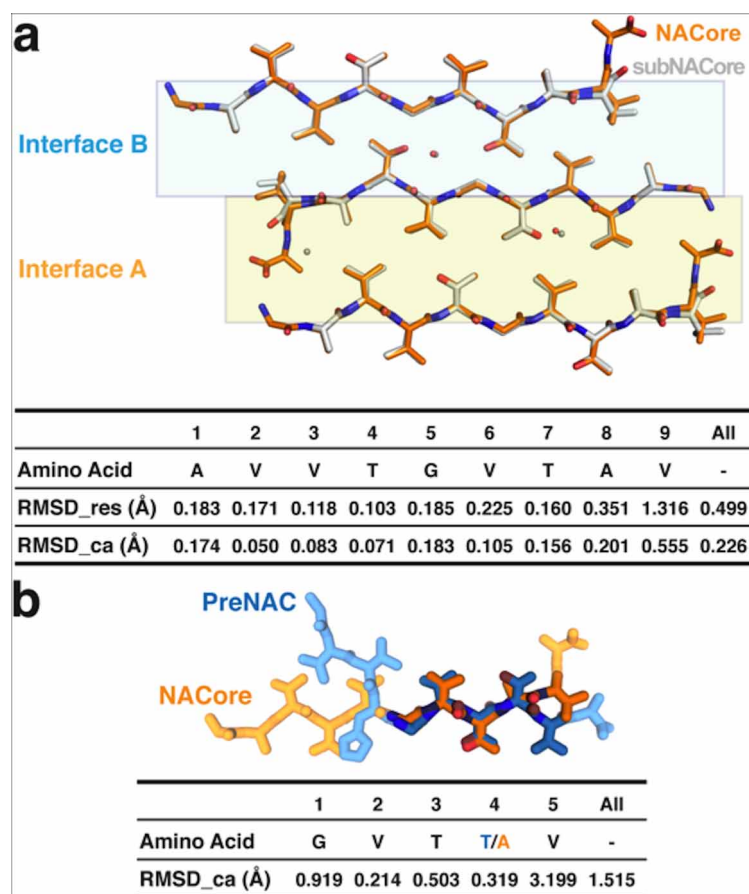
Extended Data Figure 4 | Comparison of the crystal packing for NACore and SubNACore. a, The face-to-face interactions are virtually the same for the pairs of NACore segments (orange chains) in its crystal structure and the SubNACore segments (white chains) in its structure (interfaces A and B shown in gold and blue, respectively). The table below shows the pairwise r.m.s.d. values comparing the nine residues shared in common between the structures. RMSD_res is an all-atom comparison between residue pairs, while RMSD_ca compares only Cα pairs. **b**, PreNAC (blue) is compared with NACore (orange). Five residues from each strand are shown in darker colour and the r.m.s.d. values between their Cα pairs are compared in the table below. The PreNAC–NACore interaction mimics the weaker interface B in the NACore structure.

0, 0, 2
d=8.1 A

0, 2, 0
d=2.41 A

1,1,1
d=4.59 A

-1,1,1
d=4.63 A

Extended Data Figure 5 | Intense reflections common among the NACore and the two polymorphs of full length α-synuclein suggest common structural features. Common structural features are illustrated here on the crystal packing diagrams of NACore. The (0,0,2) planes approximate the separation between sheets in interface A (orange). The (0,2,0), (−1,1,1), and (1,1,1) reflections are intense because the corresponding Bragg planes recapitulate the staggering of strands from opposing sheets. The red lines correspond to the unit cell boundaries and all planes are shown in black. The location of the unit cell origin is indicated by 'O'. The unit cell dimensions a, b, and c are labelled. Bragg spacings (spacings between planes), indicated by 'd', are indicated in angstroms.
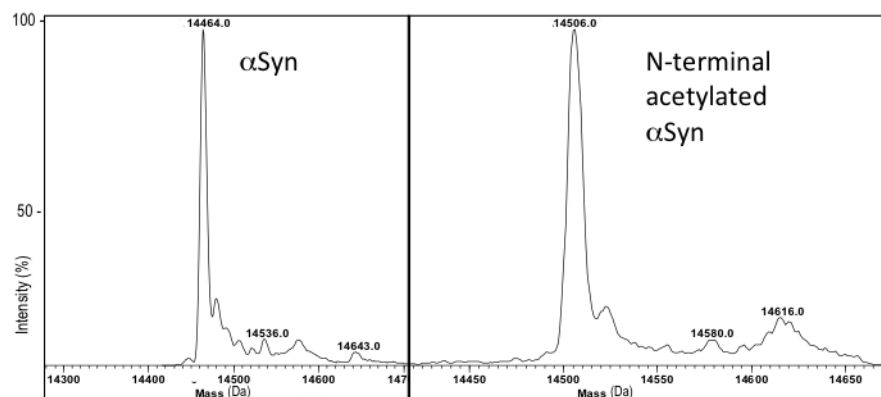
Extended Data Figure 6 | Mass spectrometry analysis of recombinantly expressed, full-length α-synuclein, with and without N-terminal acetylation. The mass profile of wild-type full length α-synuclein (left) is compared to that of an N-terminally acetylated form of the protein (right). The mass shift for the N-terminally acetylated form is appropriately shifted with respect to the native form of the protein (14464.0 Da for α-synuclein and 14506.0 Da for acetylated α-synuclein), within a margin of error of 4 Da.

Extended Data Table 1 | Statistics of data collection and atomic refinement for NACore, its fragment SubNACore, and PreNAC

Segment	SubNACore $_{69}$AVVTGVTAV$_{77}$	NACore $_{68}$GAVVTGVTAVA$_{56}$	PreNAC $_{47}$GVVHGVTTVA$_{56}$
Data collection			
Radiation source	Synchrotron	Electron	Electron
Space group	C2	C2	P21
Cell dimensions			
a,b,c (Å)	61.9, 4.80, 17.3	70.8, 4.82, 16.79	17.9, 4.7, 33.0
α,β,γ (°)	90, 104.1, 90	90, 105.7, 90	90, 94.3, 90
Resolution (Å)	1.85 (1.95-1.85)	1.43 (1.60-1.43)	1.41 (1.56-1.41)
Wavelength (Å)	0.9791	0.0251	0.0251
R_{merge}	0.117 (0.282)	0.173 (0.560)	0.236 (0.535)
$R_{r.i.m.}$	0.135 (0.322)	0.199 (0.647)	0.264 (0.609)
$R_{p.i.m.}$	0.065 (0.154)	0.093 (0.311)	0.185 (0.305)
$I/\sigma I$	5.2 (2.7)	5.5 (2.5)	4.6 (1.8)
CC$_{1/2}$ (%)	99.5 (97.8)	99.4 (92.3)	96.7(74.0)
Completeness (%)	97.9 (98.3)	89.9 (82.6)	86.9 (69.6)
Multiplicity	4.1 (4.0)	4.4 (4.3)	3.7 (3.5)
Refinement			
Resolution (Å)	1.85 (2.07-1.85)	1.43 (1.60-1.43)	1.41 (1.41-1.57)
No. reflections	470 (125)	1073 (245)	1006 (239)
R_{work}	0.176 (0.248)	0.248 (0.253)	0.235 (0.336)
R_{free}	0.221 (0.286)	0.275 (0.331)	0.282 (0.329)
CC$_{work}$	0.964 (0.896)	0.947(0.618)	0.937(0.335)
CC$_{free}$	0.889 (0.993)	0.986(0.269)	0.967(0.361)
No. atoms			
Protein	57	66	66
Water	3	2	4
B-factors (Å^2)			
Protein	17.1	9.0	16.1
Water	27.6	2.7	24.6
Wilson B (Å^2)	11.8	10.3	13.8
R.m.s deviations			
Bond lengths (Å)	0.005	0.010	0.020
Bond angles (°)	1.1	1.6	2.0
PDB ID code	4RIK	4RIL	4ZNN
EMDB ID code		EMD-3028	EMD-3001

*Highest resolution shell is shown in parenthesis. Data quality is indicated by the redundancy independent merging R factor (r.i.m) and the precision indicating merging R factor (p.i.m.).

Extended Data Table 2 | Comparison of reflections observed in powder diffraction of fibrils of full-length α-synuclein, N-acetyl α-synuclein, and a synthetic pattern calculated from our α-synuclein model, to aligned nanocrystals of NACore.

Segment	Reflections (Å)
NACore GAVVTGVTAVA	2.21, 2.26, **2.39**, 2.52, 2.61, 2.68, 2.78, 3.02, 3.12, 3.34, 3.56, 3.86, 4.34, **4.57**, 5.16, 5.98, 7.56, **8.19**, 10.46, 11.63, 13.29, 16.61
α-syn	**2.39**, **4.64**, 6.82, **8.29**, 10.06
N-acetyl α-syn	**2.38**, **4.62**, **8.18**, 9.80, 11.90
Simulated α-syn	2.23, 2.25, **2.35**, 3.29, 3.63, 3.70, 3.95, 4.08, 4.56, **4.68**, **8.36**, 8.69, 21.76, 24.47, 27.61, 31.67

Bold reflections are strong and common to all three samples. Colours of the labelled reflections match those in Fig. 2.